NASA/CR—2001-210680

Computational Aeroacoustics by the Space-Time CE/SE Method

Ching Y. Loh
Taitech, Inc., Cleveland, Ohio

National Aeronautics and
Space Administration

Glenn Research Center

February 2001

COMPUTATIONAL AEROACOUSTICS BY THE SPACE-TIME CE/SE METHOD

Ching. Y. Loh*

Taitech, Inc.
Cleveland, Ohio 44135

1 Introduction

In recent years, a new numerical methodology for conservation laws – the Space-Time Conservation Element and Solution Element Method (CE/SE), was developed by Dr. Chang of NASA Glenn Research Center and collaborators [1-3]. In nature, the new method may be categorized as a finite volume method, where the conservation element (CE) is equivalent to a finite control volume (or cell) and the solution element (SE) can be understood as the cell interface. However, due to its rigorous treatment of the fluxes and geometry, it is different from the existing schemes. The CE/SE scheme features:

(1) space and time treated on the same footing, the integral equations of conservation laws are solved for with second order accuracy,

(2) high resolution, low dispersion and low dissipation,

(3) novel, truly multi-dimensional, simple but effective non-reflecting boundary condition,

(4) effortless implementation of computation, no numerical fix or parameter choice is needed;

(5) robust enough to cover a wide spectrum of compressible flow: from weak linear acoustic waves to strong, discontinuous waves (shocks), appropriate for linear and nonlinear aeroacoustics.

Currently, the CE/SE scheme has been developed to such a stage that a 3-D unstructured CE/SE Navier-Stokes solver is already available. However, in the present paper, as a general introduction to the CE/SE method, only the 2-D unstructured Euler CE/SE solver is chosen as a prototype and is sketched in Section 2. Then applications of the CE/SE scheme to linear, nonlinear aeroacoustics and airframe noise are depicted in Sections 3, 4, and 5 respectively to demonstrate its robustness and capability.

2 the 2-D Unstructured CE/SE Scheme

The CE/SE scheme can be used with either structured or unstructured grids. Here, the unstructured CE/SE is used as a prototype for introductory description.

*e-mail:fsloh@turbot.grc.nasa.gov

2.1 Conservation Form of the Unsteady Euler Equations

Consider a dimensionless conservation form of the unsteady Euler equations of a perfect gas. Let ρ, u, v, p, and γ be the density, streamwise velocity component, transversal velocity component, static pressure, and constant specific heat ratio, respectively. The 2-D Euler equations then can be written in the following vector form:

$$\mathbf{U}_t + \mathbf{F}_x + \mathbf{G}_y = 0, \tag{1}$$

where x, y, and t are the streamwise and transversal coordinates and time, respectively. The conservative flow variable vector $\mathbf{U}$ and the flux vectors $\mathbf{F}$ and $\mathbf{G}$, are given by:

$$\mathbf{U} = \begin{pmatrix} U_1 \\ U_2 \\ U_3 \\ U_4 \end{pmatrix}, \quad \mathbf{F} = \begin{pmatrix} F_1 \\ F_2 \\ F_3 \\ F_4 \end{pmatrix}, \quad \mathbf{G} = \begin{pmatrix} G_1 \\ G_2 \\ G_3 \\ G_4 \end{pmatrix},$$

with

$$U_1 = \rho, U_2 = \rho u, U_3 = \rho v, U_4 = p/(\gamma-1)+\rho(u^2+v^2)/2;$$

$$F_1 = U_2, \quad F_3 = U_2 U_3/U_1,$$

$$F_2 = (\gamma - 1)U_4 + \left[(3 - \gamma)U_2^2 - (\gamma - 1)U_3^2\right]/2U_1,$$

$$F_4 = \gamma U_2 U_4/U_1 - (\gamma - 1)U_2\left[U_2^2 + U_3^2\right]/2U_1^2,$$

$$G_1 = U_3, \quad G_2 = U_2 U_3/U_1,$$

$$G_3 = (\gamma - 1)U_4 + \left[(3 - \gamma)U_3^2 - (\gamma - 1)U_2^2\right]/2U_1,$$

$$G_4 = \gamma U_3 U_4/U_1 - (\gamma - 1)U_3\left[U_2^2 + U_3^2\right]/2U_1^2.$$

By considering (x, y, t) as coordinates of a three-dimensional Euclidean space E_3 and using Gauss' divergence theorem, it follows that Eq. (1) is equivalent to the following integral equation:

$$\oint_{S(V)} \mathbf{H}_m \cdot d\mathbf{S} = 0, \qquad m = 1, 2, 3, 4, \tag{2}$$

where $S(V)$ denotes the surface around a volume V in E_3 and $\mathbf{H}_m = (F_m, G_m, U_m)$, $m = 1, 2, 3, 4$.

2.2 Unstructured CE/SE

The CE/SE scheme is naturally adapted to unstructured triangle grids. Each triangle center (O in $\triangle ABC$) and its 3 neighboring triangle centers (D, E, F) form 3 conservation elements or CEs (quadrilateral cylinders – $ADBO, BECO$ and $CFAO$), as shown in Fig. 1. These triangle centers are the nodes where the unknowns $\mathbf{U}, \mathbf{U_x}, \mathbf{U_y}$ are defined.

Assume that at the previous time level n (Fig. 1), $\mathbf{U}$, and its spatial derivatives $\mathbf{U}_x$, $\mathbf{U}_y$ are given at all the nodes (triangle centers), the CE/SE time marching is based on a 'tripod' mode, $i.e.$, $\mathbf{U}, \mathbf{U}_x, \mathbf{U}_y$ at the new time level $n + 1$ ($e.g.$, the shaded circle O' in Fig. 1) are computed from their data at its surrounding neighboring nodes at time level n ($e.g.$, D in Fig. 1, note that O itself is *not* used).

During the time marching, the above flux conservation relation (2) in space-time is the *only* mechanism that transfers information between node points. A conservation element CE, or computational cell, is the finite volume to which (2) is applied. Discontinuities are allowed to occur in the interior of a conservation element and nowhere else. A solution element SE associated with a node ($e.g.$, D, E, F in Fig. 1) is here a set of interface planes in E_3 that passes through this node ($e.g.$ planes $DAA'D', DBB'D', DBOA$ associated with node D). Within a given solution element $SE(j, n)$, where j, n are the node index, and time step respectively, the flow variables are not only considered continuous but are also approximated by linear Taylor expansions:

$$\mathbf{U}^*(x, y, t; j, n) = \mathbf{U}_j^n + (\mathbf{U}_x)_j^n (x - x_j) +$$

$$(\mathbf{U}_y)_j^n (y - y_j) + (\mathbf{U}_t)_j^n (t - t^n), \qquad (3)$$

$$\mathbf{F}^*(x, y, t; j, n) = \mathbf{F}_j^n + (\mathbf{F}_x)_j^n (x - x_j) +$$

$$(\mathbf{F}_y)_j^n (y - y_j) + (\mathbf{F}_t)_j^n (t - t^n), \qquad (4)$$

$$\mathbf{G}^*(x, y, t; j, n) = \mathbf{G}_j^n + (\mathbf{G}_x)_j^n (x - x_j) +$$

$$(\mathbf{G}_y)_j^n (y - y_j) + (\mathbf{G}_t)_j^n (t - t^n), \qquad (5)$$

where j is the node index of D, E or F, the partial derivatives of $\mathbf{F}$ and $\mathbf{G}$ can be related to the corresponding one of $\mathbf{U}$ by using the chain rule and $\mathbf{U}_t$ can be obtained from (1). These Taylor expansions are used to accurately evaluating fluxes on $SE's$ $e.g.$, on planes $DAA'D', DBB'D'$ or $DBOA$.

In principle, the number of equations derived from these flux conservation laws (each CE provides 4 scalar equations and the total number of scalar equations is 12) matches the number of unknowns (here 12 scalar unknowns). All the unknowns are solved for based on these relations. No extrapolations (interpolations) across a stencil of cells are needed or allowed.

In practice, there is no need to solve a 12 × 12 equation system. In the space-time E_3 space, (2) is applied to the

hexagon cylinder $ADBECF - A'D'B'E'C'F'$. U at the hexagon center at the new time level is first evaluated and then, U at the center O' of triangle $A'B'C'$ is obtained by Taylor expansion. Since the evaluation of $\mathbf{U}_x$ and $\mathbf{U}_y$ involves application of artificial damping and some form of limiters (weighted average), the reader is referred to the original papers [1-3] of Chang *et al* for details.
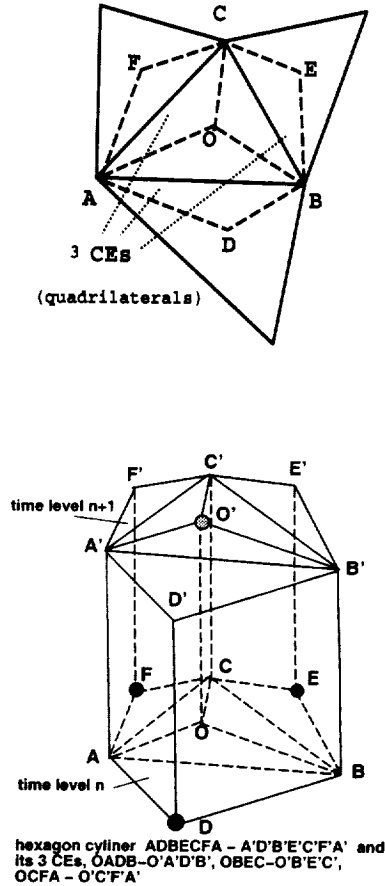

Figure 1: CE/SE unstructured grid, showing 3 CEs and the hexagon cylinder in E_3.

2.3 Non-Reflecting Boundary Conditions

In the CE/SE scheme, non-reflecting boundary conditions (NRBC) are constructed so as to allow fluxes from the interior domain to smoothly exit to the exterior of the domain. Some variants of the NRBC frequently employed in CE/SE schemes are:

(1) Type I - 'steady NRBC':

For a ghost grid node (j, n) lying outside the domain at the top (or bottom) of the domain the NRBC requires that

$$(\mathbf{U}_x)_j^n = (\mathbf{U}_y)_j^n = 0,$$

while $\mathbf{U}_j^n$ is kept fixed at the initially given steady boundary value.

(2) Type II - 'outflow NRBC':

At the downstream boundary, where there are substantial gradients in y direction, the NRBC requires that

$$(\mathbf{U}_x)_j^n = 0, \quad \mathbf{U}_j^n = \mathbf{U}_{j'}^{n-1/2} \quad (\mathbf{U}_y)_j^n = (\mathbf{U}_y)_{j'}^{n-1/2},$$

where j' is the index of an interior node closest to the boundary ghost node j and $\mathbf{U}_j^n$ and $(\mathbf{U}_y)_j^n$ are now defined by simple extrapolation from the interior. This NRBC is valid for either supersonic or subsonic flows. It should be noted that although these NRBC's bear similarity to those used in finite difference schemes, the role they play is very different. It can be shown that the above NRBC's allow fluxes to smoothly exit to the exterior of the domain.

In the following sections, the 2-D CE/SE Euler (Navier-Stokes) scheme is tested to demonstrate its capability and robustness for aeroacoustics computations. Several selected problems in linear and nonlinear aeroacoustics computations are presented. The numerical results, which cover a wide spectrum of waves, from linear and nonlinear acoustic waves to discontinuous waves (shocks), are then compared to available exact solutions or experimental ones.

3   2-D Linear Aeroacoustics Test Problems

Three typical linear aeroacoustics examples are considered in this section. More details can be found from the appropriate references.

3.1   Acoustic Pulse, Entropy Wave, and Vorticity Wave Propagation

This problem [5] is one of the benchmark problems of the first CAA Workshop (Category 3, Problem 1) [4]. The computational domain in the x-y plane is a square with $-100 \leqslant x \leqslant 100$, and $-100 \leqslant y \leqslant 100$. A uniform 201×201 grid is used with $\Delta x = \Delta y = 1$. Initially, a Gaussian acoustic pulse is located at the center of the domain ($x = y = 0$) and a weaker entropy/vorticity disturbance is located off center ($x = 67, y = 0$), with a mean flow of Mach number $M = 0.5$. The corresponding non-dimensional pressure, density, and streamwise and transverse velocity components are given by

$$p = \frac{1}{\gamma} + \delta e^{-\alpha_1(x^2+y^2)},$$

$$\rho = 1 + \delta[e^{-\alpha_1(x^2+y^2)} + 0.1\delta e^{-\alpha_2[(x-67)^2+y^2]}],$$

$$u = M + 0.04\delta y e^{-\alpha_2[(x-67)^2+y^2]},$$

$$v = -0.04\delta(x - 67)e^{-\alpha_2[(x-67)^2+y^2]},$$

where $\alpha_1 = \ln 2/9$, $\alpha_2 = \ln 2/25$, and δ is an amplitude factor. By choosing a small $\delta = 0.001$, the Euler equations are practically linearized. During the computation, the NRBC of Type-I described above is enforced at all
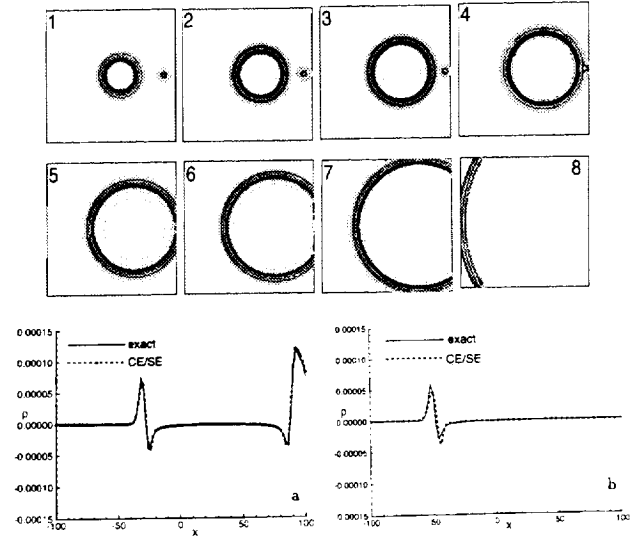

Figure 2: Propagation of an acoustic pulse with a vorticity/entropy disturbance, and comparison to exact solution.

boundaries. Fig. 2 illustrates the density contours at different time steps. It also shows that the simple NRBC is effective. Comparison of perturbed density distributions along the centerline $y = 0$ with the exact solutions at $t = 60$ and $t = 100$ are demonstrated in Plots (a) and (b) respectively. The numerical results agree well with the theoretical ones, with no visible dispersion error.

3.2   Linear Instability of a Free Shear Layer and Vortex Roll-Up

In the 2nd example [5], the inviscid linear and nonlinear instability properties of a free shear layer is studied. The numerical results are compared with linear results obtained by the normal mode approach.

The background mean flow consists of a fast (supersonic) stream on the top half domain and a slow (subsonic) stream at the bottom half, with the two parallel streams connected by a shear layer of hyperbolic tangent shape. The nondimensional flow states are given as:

$$U_1 = 1, V_1 = 0, \quad p_1 = 1/3.15, \quad \rho_1 = 1,$$

$$U_2 = .7391304, V_2 = 0, \quad p_2 = 1/3.15, \quad \rho_2 = 0.5405405.$$

The computational domain spans between $0 \leqslant x \leqslant 300$ and $-10 \leqslant y \leqslant 10$, with a uniform structured grid of 601×101 (1201×201 for fine grid), with time step size $\Delta t = 0.15$. The computation is carried out until $t = 390$ when the spatial instability is fully developed. A small harmonic perturbation (amplitude $\delta = 0.001$) at the most unstable frequency $f = 0.062$ is enforced at the inlet boundary. Fig. 3 shows the power spectrum P_n of the computed
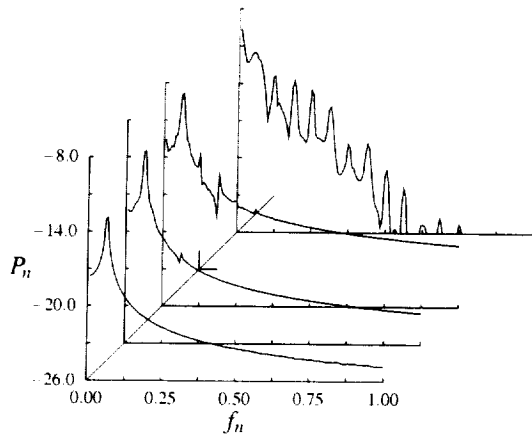
Figure 3: Power spectra at $x = 050, 100, 150,$ and 250 with forcing at the most unstable frequency according to linear theory: (coarse grid)

u' (perturbed u) in natural log scale at the streamwise stations $x = 50, 100, 150,$ and 250, which correspond to about $3.5, 7$ wavelengths and so on. At $x = 50$, there is a clearly discernable peak centered about the forcing frequency $f = 0.062$. At about $x = 100$, second and third harmonics start to emerge. Further downstream, more harmonics appear and eventually the fundamental saturates. The streamwise evolution of the disturbance ampli-
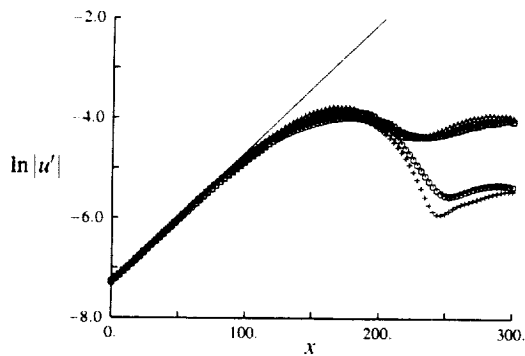
Figure 4: Streamwise evolution of disturbance amplitude with forcing at the most unstable frequency according to linear theory ($f = .062$). Squares: total u_{rms}, coarse grid; triangles: total u_{rms}, finer grid: circles: u_{rms} at forcing frequency, coarse grid; crosses: u_{rms} at forcing frequency, finer grid; solid line: linear growth.

tude along the horizontal centerline $y = 0$ is illustrated in Fig 4. Numerical results for both the coarse and fine grids are presented and compared to the theoretical linear growth. It is seen that for $0 \leqslant x \leqslant 100$ (about 7 wavelengths) the coarse-grid and fine-grid computations yield good agreement both between themselves and with the linear result. Further downstream, nonlinear effects become

important, the growth rate is reduced from the linear value, and ultimately the fundamental saturates. Both numerical results agree reasonably well with each other also in this nonlinear region. Fig. 5 shows the streamwise evolution of
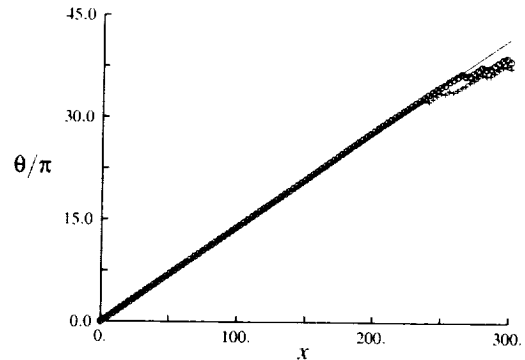

Figure 5: Streamwise evolution of disturbance phase with forcing at the most unstable frequency according to linear theory (f=.062). Circles: coarse grid; crosses: finer grid: solid line: linear result.

the disturbance phase. The numerical results for both the coarse and finer grids are compared to the corresponding result from linear theory. The agreement is surprisingly good until well into the nonlinear region. Fig. 6 compares
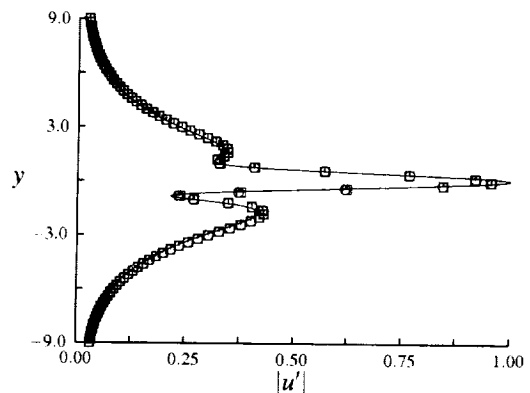

Figure 6: Transverse mode shape at $x = 100$ with forcing at most unstable frequency according to linear theory, finer grid. Squares: total u_{rms}: circles: u_{rms} at forcing frequency; solid line: linear eigenfunction (modulus).

the normalized $|u'|$ profile across the shear layer flow with the eigenfunction from linear stability theory at the streamwise station $x = 100$, which is located towards the end of the linear growth region. The agreement is excellent. The phase variation across the shear layer of the disturbance at the same station is depicted in Fig. 7. Fig. 8 shows the contours of the flow variables for the finer-grid computation. This figure clearly demonstrates the effectiveness of
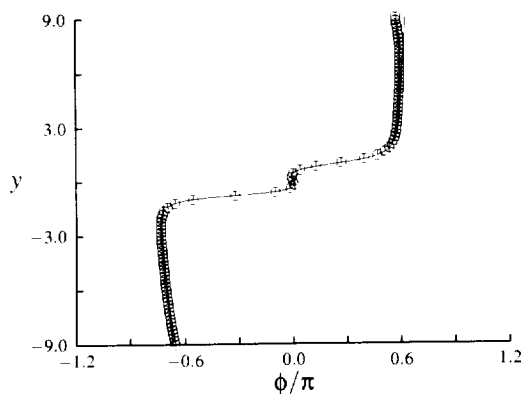
Figure 7: Transverse phase variation at $x = 100$ with forcing at most unstable frequency $f = .062$ according to linear theory, (fine grid). Circles: u_{rms} at forcing frequency; solid line: linear eigenfunction (phase).

Figure 8: Flow variable contours at $t = 390$, fine grid

the NRBC's at the top, bottom and outlet. It should be emphasized that the domain shown in the figures is exactly the computational domain, no buffer zones, cut-offs or other numerical fixes are applied.

3.3 Mach radiation of a fully expanded axisymmetric jet

Another interesting linear or quasi-linear wave phenomenon is the Mach radiation from a fully expanded supersonic jet. In the following examples, a perturbation (or forcing) is provided by a right-hand-side source term in the energy equation, the 4th component of Eq. (1), located at the origin $(0, 0)$ inside the jet core:

$$\frac{\delta}{\gamma - 1} \exp[-B(x^2 + y^2)] \cos(\omega t),$$

where δ is a small number $(0.00005 < \delta < 0.001)$, $\omega = 2\pi St$, and the constant $B = 8$.

3.3.1 *Mach radiation from a supersonic axisymmetric jet* In this test example [6], a fully expanded supersonic jet with Mach number $M_j = 2.0$ is considered. The computational domain spans between $0 \leqslant x \leqslant 33D$ and $0 \leqslant y \leqslant 19D$, with a non-uniform structured grid of 350×281 nodes, where D is the diameter of the jet at the nozzle exit. More grid points are packed around the shear layer. The perturbation source strength $\delta = 0.001$. The computation of the unsteady jet flow is carried out to $t = 100$ when the spatial instability is fully developed. Fig. 9 illustrates the isobars and v-velocity contours in the near and intermediate field. The Mach radiation flow pattern agrees qualitatively with experimental [14] and other computational [15] results.

3.3.2 *Mach wave system inside the jet (M=1.2)*
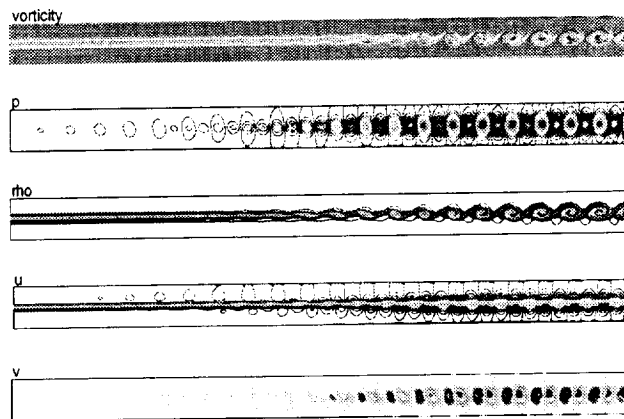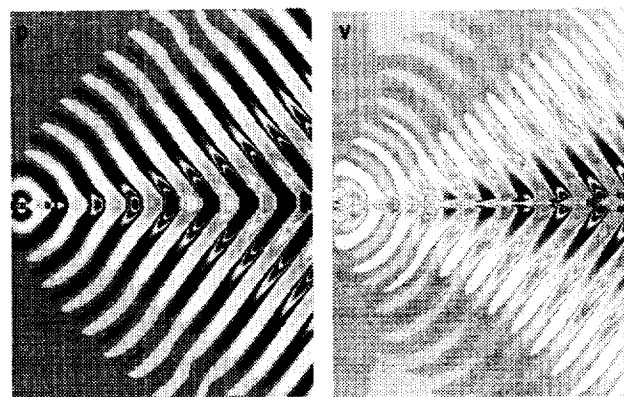It was found that, as analyzed by Tam and Hu [7], the

Figure 9: Type I Mach radiation of a supersonic jet at $M_j = 2.0$ and Strouhal number $St = 0.2$, domain size 33Dx19D, non-uniform grid.

Mach radiation attenuates exponentially outside the jet shear layer, while the Mach wave system is trapped inside the jet and forms a cross-hatch pattern. Here the jet shear layer plays the role as a 'wave guide'.

The computational domain is $0 \leqslant x \leqslant 3D$ and $0 \leqslant y \leqslant 1D$, with a non-uniform grid of 331×101 nodes, where again D is the diameter of the jet at the nozzle exit. The perturbation source strength $\delta = 0.00005$, with a high Strouhal number $St = 2.0$. A time step size $\Delta t = 0.0015$ is chosen. The computation of the unsteady jet flow is carried out for 12000 steps to ensure that the spatial instability is fully developed.

Fig 10 clearly demonstrates the cross-hatch pattern of the Mach wave system inside the 'wave guide'—the jet core. The Mach waves are repeatedly reflected because they do not penetrate the annular shear layer. The pat-
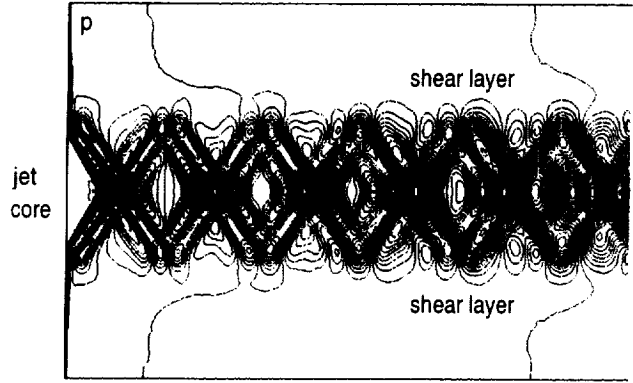
M_j=1.2, 3Dx1D, 300x100 grid, St. =2. dt=.0015,ee=.00005; showing cross-hatching Mach wave system.

Figure 10: Mach wave system within a supersonic jet of $M_j = 1.2$ at high Strouhal number $St = 2.0$, isobars show the cross-hatch pattern.

tern qualitatively agrees with the analysis of Tam and Hu [7]. At a low supersonic Mach number $M_j = 1.2$, at the outer surface of the shear layer, the local phase velocity can hardly exceed the local speed of sound and hence practically no exterior Mach radiation occurs.

4 2-D Non-linear aeroacoustics Test problems

In this section, two examples of non-linear aeroacoustics involving shocks are considered. For the first example, more details can be found from [5].

4.1 Multiple Interaction of a Strong Vortex and Shocks

Vortex-shock interaction has been considered a 'difficult' problem for CAA. However, the CE/SE Euler scheme can solve the problem in an effortless way, without any numerical trick or fix [5]. As seen in Fig 11, a uniform structured grid of 401 × 101 nodes is employed in the rectangular domain with $\Delta x = \Delta y = 1$. The inflow boundary condition is given as a supersonic flow with a Mach number of 2.9:

$$u_0 = 2.9, \quad v_0 = 0, \quad p_0 = 1/1.4, \quad \rho_0 = 1.$$

The boundary condition at the top is an inclined flow:

$$u_t = 2.6193, \quad v_t = -0.50632, p_t = 1.5282, \quad \rho_t = 1.7000.$$

The outflow boundary condition is the type-II NRBC and the bottom is a solid reflecting wall. Then, a steady oblique shock is formed with 29° inclination and reflected at the bottom wall. The flow with shocks is pre-calculated until a steady state is reached. It is then used as the background mean flow for further computation.

At $t = 0$, a strong Lamb's vortex is placed at $x = 22, y = 60$. With $\Delta t = 0.2$, 900 time steps were run.

Fig. 11 demonstrates the shock-vortex interaction at the different times $t = 2, 20, 38, 56, 74, 92, 110, 128, 146,$ and 180, and shows how the nonlinear acoustic waves are generated, and how they pass through the shocks and convect downstream.
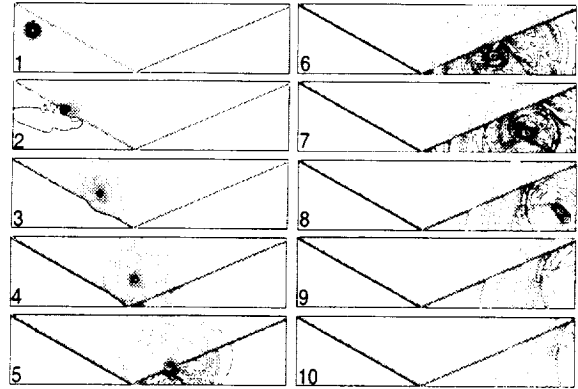
isobars for a vortex passing through shocks, with acoustic waves generated.

Figure 11: Multiple interactions of a strong vortex and shocks producing nonlinear acoustic waves.

4.2 Screech tone noise of an underexpanded jet

In nature, the screech noise is caused by an acoustic feedback loop between the jet nozzle exit lip (or nearby solid surfaces) and the shock cell structure. At the low supersonic jet Mach number $M_j = 1.19$, the overall motion in the experiment [8] is in an axisymmetric mode, and the use of axisymmetric 2-D scheme is appropriate.

The Navier-Stokes CE/SE solver with LES (large eddy simulation) is applied to a triangular unstructured grid of 88300 elements (cells). The geometry of the computa-
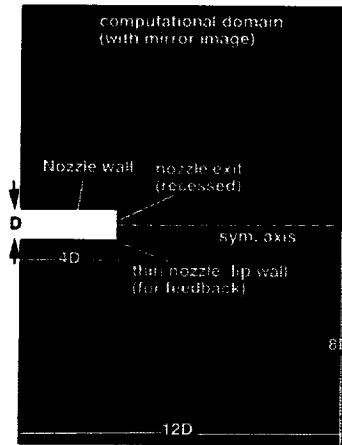

Figure 12: Geometry of the computational domain.

tional domain is shown in Fig 12. Both Type I and II

NRBC's are applied appropriately to all boundaries except at the nozzle solid walls where no-slip solid wall boundary condition is employed, and at the nozzle exit where the following inflow condition is applied:

$$p_e = p_0 \left[\frac{1 + \frac{1}{2}(\gamma - 1)M_j^2}{1 + \frac{1}{2}(\gamma - 1)} \right]^{\frac{\gamma}{\gamma-1}} ,$$

$$\rho_e = 0.5(\gamma + 1)\rho_0 \left[\frac{1 + \frac{1}{2}(\gamma - 1)M_j^2}{1 + \frac{1}{2}(\gamma - 1)} \right]^{\frac{\gamma}{\gamma-1}} ,$$

$$u_e = (\frac{2}{(\gamma + 1)})^{1/2}, v_e = 0.$$

Initially the entire field is set to the ambient flow:

$$\rho_0 = 1, \quad u_0 = 0, \quad v_0 = 0, \quad p_0 = \frac{1}{\gamma}.$$

In the numerical simulation, the initial impact of the boundary condition at the nozzle exit will stimulate the jet shear layer and trigger the feedback loop to form the self-sustaining oscillation that generates screech waves.
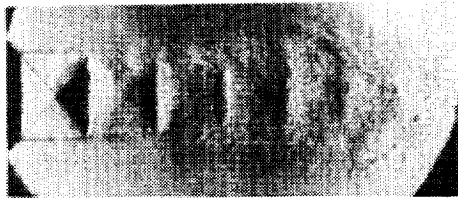

Figure 13: Schlieren picture from experiment (Panda), showing shock cells.

Fig. 14 illustrates the radiating screech waves at the time level of 212,800 steps. Since there is no forcing at all, these waves are a sure sign of the presence of a sustainable self-excited oscillation. In the processing of the numerical data for this figure, the very high level isobar contours, corresponding to hydrodynamic waves around the jet core area are 'cut off' and the 'colors' are appropriately adjusted so that the acoustic waves are clearly displayed. The screech wavelength is about $1.6D$, well in line with experimental results (e.g. [8]) and theoretical predictions (e.g. Seiner [10], Tam [9]). The shock cell structure in Fig. 14 is comparable to the experimental Schlierens in Fig. 13. Fig. 15 shows the PSD (power spectrum density) at the location $(x = 2.0, y = 6.0)$. It is seen that the spikes at the fundamental frequency and the subharmonics shoot out against the background noise, despite the low resolution. The fundamental frequency is estimated to be about $8,661$ Hz in this case, comparable to the experimental case - 8,425 Hz.

M_j =1.19 axisym. jet, isobar at time step 212800, showing shock cell structure and screech waves

Figure 14: Screech wave radiation and shock cell structure (numerical Schlierens).

5 The Airframe Noise Problems

Airframe noise is an important noise source in aeroacoustics. Several airframe tone noise problems are considered in this section to demonstrate the capability of the CE/SE scheme.

5.1 The subsonic cavity noise problem

In this problem[11], a $M = 0.8$ subsonic flow passes over a cavity of aspect ratio 6.5. Tonal oscillations occur in a feedback cycle in which the vortices shed from the upstream lip of the cavity convect downstream and impinge on the other lip, generating acoustic waves that in turn propagate upstream to excite new vortices (Fig 16).

In the computational domain, 42,000 triangular elements are used in the unstructured grid, which is made from structured rectangular cells. Figure 17 depicts with isobars where the acoustic waves are generated and propagate in a series of snapshots (1-12) in the near field of the cavity. Each snapshot is 3.6 (720 steps) unit apart in time. Initially, the flow conditions are set to be identical to the ambient flow. The boundary conditions are the appropriate types of NRBC except at the cavity walls, where slip, reflective wall boundary condition is applied. No visible reflections are observed at the non-reflecting bound-
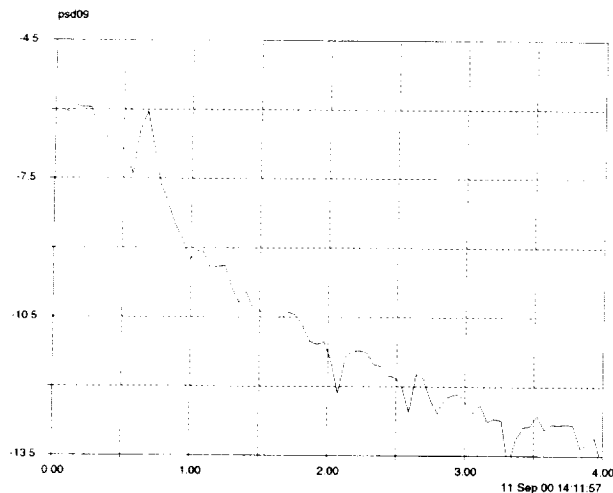
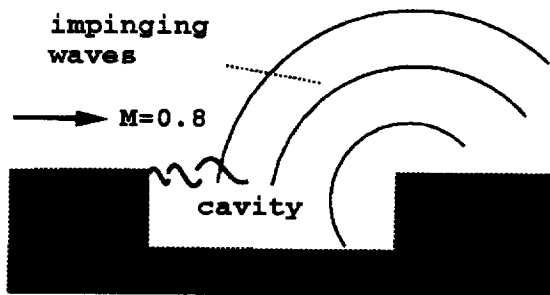Figure 15: PSD at $(x = 2.0, y = 6.0)$; x-axis: Strouhal number.

Figure 16: Sketch of the subsonic cavity noise problem.

Isobar snapshots, showing generation of near field non-linear acoustic waves around the cavity.

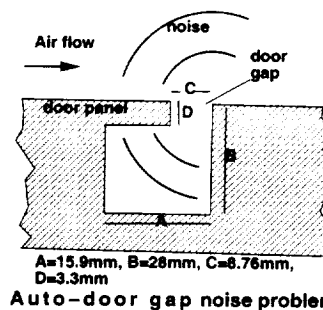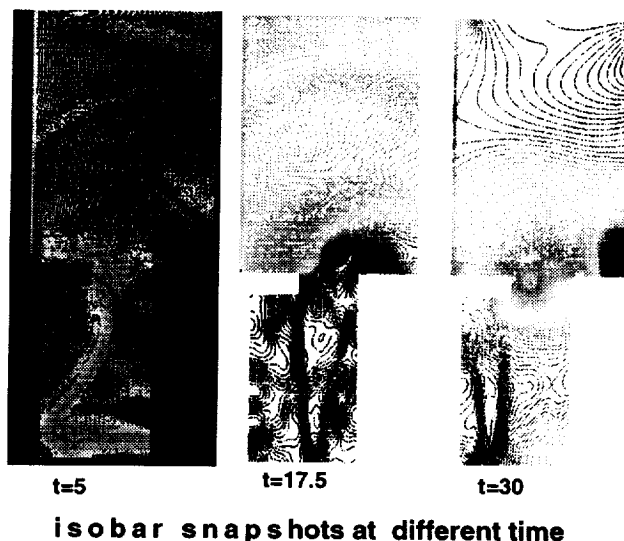Figure 17: Isobar snapshots of the subsonic cavity flow field.

A=15.9mm, B=28mm, C=8.76mm, D=3.3mm

Auto-door gap noise problem

Figure 18: Sketch of the auto-door gap noise problem with actual sizes.

aries. At the inflow boundary, upstream propagating waves are well absorbed within 2 cells, without contaminating the interior domain. From an animation of the solution, the near field acoustic wave structure appears to be complicated and chaotic.

5.2 Auto-door gap noise

Figure 18 illustrates the geometric configuration of the door gap noise problem, which represents a typical cavity aeroacoustic feedback system. The problem is given as a benchmark problem at the 3rd CAA Workshop [12] (OAI/NASA Glenn, Cleveland, OH, November, 1999). 2C ($17.52mm$) is chosen as the length scale and the speed of sound and density of the ambient flow are respectively the scales for velocity and density. In the current computation, there are 48,184 triangle elements for the unstructured mesh in the computational domain. These triangles are actually obtained by dividing a rectangular structured mesh cell into 4 pieces. The rectangular cell keeps a uniform size of $\Delta x = 0.00625$ and $\Delta y = 0.01136$ around the area of the gap and the interior of the cavity, but grows larger near the boundaries. The mean flow follows the x-direction with Mach number $M = 0.1497$, corresponding

isobar snapshots at different time

Figure 19: Isobar snapshots at various time steps in the flow field, showing formation of vortices.
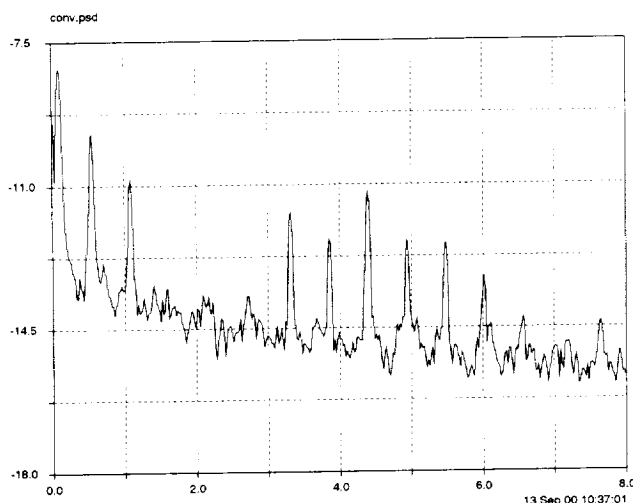
Figure 20: PSD at the midpoint of the left wall of the door gap cavity; x-axis: Strouhal number, y-axis: PSD in log. scale.

to the car speed of $50.9m/s$. Initially, ambient flow condition is imposed on the entire flow field. At the inflow, the $M = 0.1497$ flow is imposed. At the top and bottom the Type I NRBC is used while at the outflow, the Type II NRBC is specified. The domain shown in Fig. 19 is exactly the computational domain, no buffer zone is used but still, the CE/SE NRBC is very effective. The generation of vortices and the generation of (nonlinear) acoustic waves by vortex- gap edge impingement, both inside and outside of the cavity, are clearly displayed. The computation is totally carried out for $225,000$ time steps. Starting from time step 60,000, when the unsteady flow is considered as fully developed, the pressure history at the mid-point of the left wall of the cavity is recorded and provides for FFT (fast Fourier transform) analysis. Fig. 20 displays the PSD (power spectrum density) in log. scale for the time series. The $x-$ axis denotes the reduced frequency – the Strouhal numberSt. $St = 1$ is equivalent to a frequency of $19,406$ Hz. It is observed that there are several different tone spikes extending to very high frequencies. The frequency at the lowest tone spike is at 1839 Hz. This agrees well with the experimental frequency data (1824 Hz) provided by the 3rd CAA Workshop.

5.3 Blunt trailing edge noise

In this last example, the noise generated by the von Karman vortex street downstream of a rectangular blunt slab is computed. The flow Mach number is $M = 0.3$. Figure 21 illustrates the details of the computational domain. Initially, the entire field is set at the ambient flow. Then the inflow of $M = 0.3$ is imposed at the left boundaries. At the solid slab walls, no-slip condition is applied. The computation is totally carried out for $390,000$ time steps. Time

isobars at t=390,000 steps, showing von Karman vortex street at the trailing edges of a blunt slab (unstructured grid w. 77,600 triangles, dt=.005)
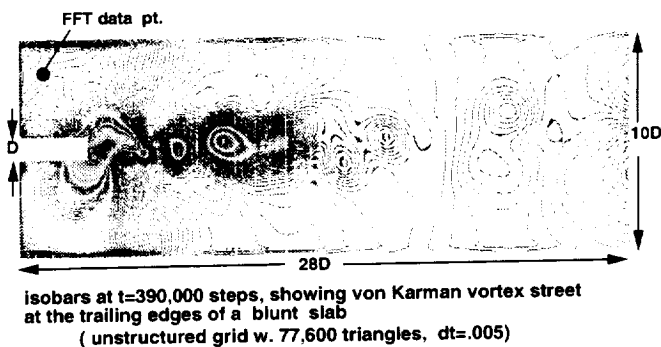
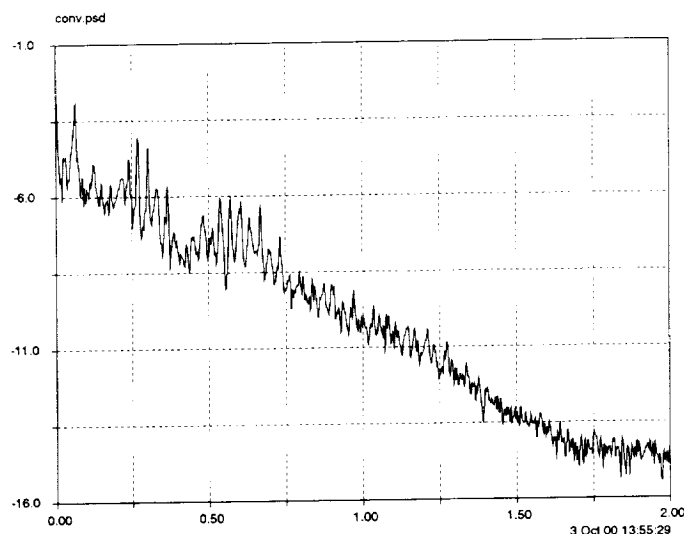Figure 21: Isobar snapshot, showing von Karman vortex street downstream of the slab.

Figure 22: PSD at the FFT data point; x-axis: Strouhal number.

history at the data point as shown in Fig. 21 is recorded for FFT analysis. The power spectrum density (PSD) is shown in Fig. 22. As before, the $x-$ axis denotes the reduced frequency – the Strouhal numberSt. $St = 1$ is equivalent to a frequency of $13,386$ Hz if the thickness of the slab is assumed to be one inch. The frequency at the lowest tone spike is 784 Hz. Although there is currently no experimental data known to the author, this frequency doesn't seem to be in conflict with other experiments, e.g., a $M = 0.2$ flow past a circular cylinder of diameter $1.9cm$, with the frequency of $f = 643$ Hz (the 2nd CAA Workshop, Category 4 [13]).

6 Concluding remarks

Through numerous numerical examples, the capability of the new CE/SE schemes is demonstrated. The CE/SE scheme is a time-accurate conservative scheme for CFD and CAA. Its features include:

(1) naturally adapted to unstructured grid,

(2) high resolution, low dispersion, and low dissipation, despite its nominal 2nd order accuracy (in space and time),

(3) robust, treats the 'difficult' problems in a simple, effortless way, particularly appropriate for near field, nonlinear aeroacoustics,

(4) the novel NRBC is simple, effective and truly multidimensional.

In the near future, 3-D LES or turbulence modeling will be considered in the CE/SE scheme development.

References

[1] Chang, S. C., "The Method of Space-Time Conservation Element and Solution Element—A New Approach for Solving the Navier-Stokes and Euler Equations," Journal of Computational Physics. v. 119, 295-324 (1995).

[2] Chang, S.-C., Wang, X.-Y. and Chow, C.-Y., "The Space-Time Conservation Element and Solution Element Method: A New High Resolution and Genuinely Multidimensional Paradigm for Solving Conservation Laws ", J. Comp. Phys. v.156, 89-136 (1999).

[3] Wang, X.Y. and Chang, S.C. "A 2D Non-splitting Unstructured Triangular Mesh Euler Solver Based on the Space-Time Conservation Element and Solution 'Element Method ", CFD Journal,vol. 8, pp.309-325, 1999. (1998).

[4] Hardin, J. C., Ristorcelli, and Tam, C. W. (Eds.), "ICASE/LaRC Workshop on Benchmark Problems in Computational Aeroacoustics", Hampton, VA. 1994, NASA CP 3300.

[5] Loh, Ching Y., Hultgren, Lennart S. and Sin-Chung Chang, "Computing Waves in Compressible Flow Using the Space-Time Conservation Element Solution Element Method," AIAA Paper 98-0369 (1998), also to appear in AIAA Journal.

[6] Loh, C. Y., Hultgren, L. S., Wang,Xiao Y., Chang, S.-C. and Jorgenson, P. C. E., "Aeroacoustics Computation for Nearly fully Expanded Supersonic jets Using the CE/SE Method", AIAA Paper 2000-2010 (2000).

[7] Tam, C. K. W, and Hu, F. Q., "On the three families of instability waves of high-speed jets", J. Fluid Mech., vol. 201, pp. 447-483 (1989).

[8] Panda, J., "An experimental investigation of screech noise generation," J. Fluid Mech., v. 378, pp. 71-96 (1998).

[9] Tam, C. K .W., "Supersonic Jet Noise," Ann. Rev. Fluid Mech. v. 27, pp. 17-43 (1995).

[10] Seiner, J. M., "Advances in High Speed jet Aeroacoustics," AIAA Paper 84-2275 (1984).

[11] Loh, C. Y., Wang,Xiao Y., Chang, S.-C. and Jorgenson, P. C. E., " Computation of Feedback Aeroacoustic System by the CE/SE Method" Presented at the 1st International CFD Conference, July, 2000, Kyoto, Japan.

[12] " The Third Workshop on Benchmark Problems in Computational Aeroacoustics", OAI/NASA Glenn, Ohio, U.S.A. (Nov.,1999), in press.

[13] Tam, C.K.W. and Hardin,J.C.(Eds.), " Second Computational Aeroacoustics Workshop on Benchmark Problems", Tallahassee, Nov., 1996; NASA CP 3352.

[14] Troutt, T. R. and McLaughlin, D. K., " Experiments on the flow and acoustic properties of a moderate-Reynolds-number supersonic jet", J. Fluid Mech., vol. 116, pp. 123-156 (1982).

[15] Shih, S. H., Hixon, D. R. and Mankbadi, R. R., "Zonal Approach for Prediction of Jet Noise", AIAA J., vol.13, pp. 745-752 (1997).

REPORT DOCUMENTATION PAGE

Public reporting burden for this collection of information is estimated to average 1 hour per response, including the time for reviewing instructions, searching existing data sources, gathering and maintaining the data needed, and completing and reviewing the collection of information. Send comments regarding this burden estimate or any other aspect of this collection of information, including suggestions for reducing this burden, to Washington Headquarters Services, Directorate for Information Operations and Reports, 1215 Jefferson Davis Highway, Suite 1204, Arlington, VA 22202-4302, and to the Office of Management and Budget, Paperwork Reduction Project (0704-0188), Washington, DC 20503.

1. AGENCY USE ONLY (Leave blank)	2. REPORT DATE February 2001	3. REPORT TYPE AND DATES COVERED Final Contractor Report

4. TITLE AND SUBTITLE

Computational Aeroacoustics by the Space-Time CE/SE Method

5. FUNDING NUMBERS

WU–708–90–43–00
NAS3–97186

6. AUTHOR(S)

Ching Y. Loh

7. PERFORMING ORGANIZATION NAME(S) AND ADDRESS(ES)

Taitech, Inc.
21000 Brookpark Road
Cleveland, Ohio 44135

8. PERFORMING ORGANIZATION REPORT NUMBER

E–12523–1

9. SPONSORING/MONITORING AGENCY NAME(S) AND ADDRESS(ES)

National Aeronautics and Space Administration
Washington, DC 20546–0001

10. SPONSORING/MONITORING AGENCY REPORT NUMBER

NASA CR—2001-210680

11. SUPPLEMENTARY NOTES

12a. DISTRIBUTION/AVAILABILITY STATEMENT

Unclassified - Unlimited
Subject Categories: 02, 64, and 71   Distribution: Nonstandard

Available electronically at http://gltrs.grc.nasa.gov/GLTRS

This publication is available from the NASA Center for AeroSpace Information, 301–621–0390.

12b. DISTRIBUTION CODE

13. ABSTRACT (Maximum 200 words)

In recent years, a new numerical methodology for conservation laws—the Space-Time Conservation Element and Solution Element Method (CE/SE), was developed by Dr. Chang of NASA Glenn Research Center and collaborators. In nature, the new method may be categorized as a finite volume method, where the conservation element *(CE)* is equivalent to a finite control volume (or cell) and the solution element *(SE)* can be understood as the cell interface. However, due to its rigorous treatment of the fluxes and geometry, it is different from the existing schemes. The CE/SE scheme features: (1) space and time treated on the same footing, the integral equations of conservation laws are solved for with second order accuracy, (2) high resolution, low dispersion and low dissipation, (3) novel, truly multi-dimensional, simple but effective non-reflecting boundary condition, (4) effortless implementation of computation, no numerical fix or parameter choice is needed, and (5) robust enough to cover a wide spectrum of compressible flow: from weak linear acoustic waves to strong, discontinuous waves (shocks), appropriate for linear and nonlinear aeroacoustics. Currently, the CE/SE scheme has been developed to such a stage that a 3-D unstructured CE/SE Navier-Stokes solver is already available. However, in the present paper, as a general introduction to the CE/SE method, only the 2-D unstructured Euler CE/SE solver is chosen as a prototype and is sketched in Section 2. Then applications of the CE/SE scheme to linear, nonlinear aeroacoustics and airframe noise are depicted in Sections 3, 4, and 5 respectively to demonstrate its robustness and capability.

14. SUBJECT TERMS

Aeroacoustics; CE/SE method

15. NUMBER OF PAGES
16

16. PRICE CODE
A03

17. SECURITY CLASSIFICATION OF REPORT	18. SECURITY CLASSIFICATION OF THIS PAGE	19. SECURITY CLASSIFICATION OF ABSTRACT	20. LIMITATION OF ABSTRACT
Unclassified	Unclassified	Unclassified	

NSN 7540-01-280-5500